

**Analytical Gradient Theory for Resolvent-Fitted Second-Order Extended  
Multiconfiguration Perturbation Theory (XMCQDPT2)**

Jae Woo Park\*

*Department of Chemistry, Chungbuk National University (CBNU), Cheongju 28644, Korea*

**Abstract**

We present the formulation and implementation of an analytical gradient algorithm for extended multiconfiguration quasidegenerate perturbation theory (XMCQDPT2) with the resolvent-fitting approximation by Granovsky. This algorithm is powerful when optimizing molecular configurations with a moderate-sized active space and many electronic states. We demonstrate the utility of the current algorithm in optimizing the minimum energy conical intersection (MECI) geometries of the retinal chromophore model RPSB6 and evaluating nuclear gradients when there are many electronic states. Furthermore, we parallelize the algorithm using the OpenMP/MPI hybrid approach. Additionally, we report the computational cost and parallel efficiency of the program.

---

\* E-mail: jaewoopark@cbnu.ac.kr

## 1. INTRODUCTION

Multireference perturbation theories (MRPTs) are an efficient means to recover dynamical correlations from multiconfiguration self-consistent field (MCSCF) reference functions. There are many MRPT variants: complete active space perturbation theory (CASPT),<sup>1,2</sup>  $N$ -electron valence state perturbation theory (NEVPT),<sup>3-5</sup> multireference Møller–Plesset perturbation theory (MRMP)<sup>6-8</sup> and its multistate extension, multiconfiguration quasidegenerate perturbation theory (MCQDPT)<sup>6-9</sup>, which are among the most widely used. MRPTs are classified into internally contracted and uncontracted methods. Internal contraction means that the first-order interacting space (FOIS) is formed by applying excitation operators onto the reference states. For example, CASPT2, SC- and PC-NEVPT2 are internally contracted, while UC-NEVPT2 and MCQDPT2 are uncontracted.

The availability of analytical nuclear gradients expands the utility of quantum chemical methods, particularly in applications using geometry optimizations and molecular dynamics simulations.<sup>10-13</sup> For internally contracted theories, analytical gradient methods were developed for CASPT2,<sup>14-22</sup> NEVPT2,<sup>23-26</sup> and, most recently, RASPT2.<sup>27</sup> The internal contraction somewhat complicates the mathematical formulation of the theories, and the first development of the analytical gradient for MRPTs occurred in MCQDPT2 by Nakano, Hirao, and Gordon.<sup>28,29</sup> Recently, we reported its applications in conical intersection optimizations of photochemical systems.<sup>30</sup>

The computational cost for evaluating the energy and nuclear gradient of MCQDPT2 is usually higher than the cost of CASPT2 and NEVPT2, as MCQDPT2 is an uncontracted theory. The computational cost depends on the size of the active space  $N_{\text{act}}$  and the number of electronic configurations  $N_{\text{det}}$ . The most expensive term dependent on  $N_{\text{det}}$  in CASPT2 and NEVPT2 nuclear

gradient evaluation is the four-particle reduced density matrix (4RDM), which scales as  $N_{\text{det}}N_{\text{act}}^8$ . In XMCQDPT2 nuclear gradient evaluation, on the other hand, the most expensive term scales as  $N_{\text{state}}^2N_{\text{det}}N_{\text{act}}^6(N_{\text{vir}} + N_{\text{closed}})$ .<sup>30</sup> In many CASCI problems,  $N_{\text{vir}} + N_{\text{closed}} > N_{\text{act}}^2$ , and treating systems with a moderate active space is usually impractical with MCQDPT2.

Two notable improvements over the original MCQDPT2 regarding the accuracy and computational efficiency were achieved by utilization of the “extension” and the resolvent fitting, respectively, both by Granovsky.<sup>31,32</sup> In the extended MCQDPT2 (XMCQDPT2), one uses the eigenstates of the Fock operator rather than the electronic Hamiltonian as the reference states, which results in the correct description of the potential energy surfaces near the surface crossing points. The resolvent-fitting (or table-driven) approach decouples  $N_{\text{det}}$  and  $N_{\text{vir}}$  in the computational cost by introducing interpolation with  $N_{\text{grid}}$  interpolation grids, reducing the computational cost of the most expensive term to  $N_{\text{grid}}(N_{\text{core}} + N_{\text{vir}})N_{\text{act}}^6 + (N_{\text{fgrid}} + N_{\text{state}})N_{\text{act}}^6N_{\text{det}}N_{\text{state}}$ , where  $N_{\text{fgrid}}$  grid points are included in the interpolation.<sup>32</sup> These contributions made (X)MCQDPT2 applicable to large systems with a large active space, a state-averaging space, and basis functions.

In this work, we develop an analytical nuclear gradient theory for XMCQDPT2 with resolvent fitting. The analytical gradient is readily computed with moderate-sized active spaces up to (12e, 12o) with this approximation. As numerical examples, we apply the theory to optimize the conical intersections of the retinal model chromophore RPSB6. We also demonstrate the applicability of the current algorithm for computing analytical gradients with many electronic states. Finally, we test the efficiency of the energy and nuclear gradient algorithms with OpenMP/MPI hybrid parallelization.

## 2. THEORY

This section first briefly overviews (X)MCQDPT2<sup>9,31,33</sup> with resolvent fitting and introduces its gradient theory. For readability, we closely follow the notation in the original MCQDPT2 paper by Nakano.<sup>9</sup> Namely,  $P, Q, \dots, \alpha, \beta, \dots, A, B, \dots, i, j, \dots, a, b, \dots, e, f, \dots, p, q, \dots$  denote the XMCQDPT2 states, reference states, Slater determinants, doubly occupied (inactive) orbitals, active orbitals, virtual orbitals, and general orbitals, respectively. Our implementation is based on Slater determinants but is also applicable for (X)MCQDPT2 implementations based on configuration state functions (CSFs).

**Brief Overview of (X)MCQDPT2.** In (X)MCQDPT2, the electronic Hamiltonian is partitioned into

$$\hat{H} = \hat{H}^{(0)} + \hat{V}. \quad (1)$$

The zeroth-order Hamiltonian is defined as

$$\hat{H}^{(0)} = \hat{P}\hat{f}\hat{P} + \hat{Q}\hat{f}\hat{Q}, \quad (2)$$

where  $\hat{P}$  is a projector to the reference space and  $\hat{Q}$  is a projector to the expansion basis. The one-electronic Fock operator is defined as

$$\hat{f} = \sum_{pq} f_{pq} \hat{E}_{pq} = \sum_p \varepsilon_p \hat{E}_{pp}, \quad (3)$$

where the orbitals are semicanonicalized (in which the inactive-inactive, active-active and virtual-virtual blocks are diagonalized). Note that although the semicanonical orbitals are the most natural choice for the active orbitals, the first implementation of MCQDPT2 did not stick to the semicanonical active orbitals but also used natural orbitals.<sup>9</sup> The effective Hamiltonian is constructed as

$$H_{\alpha\beta}^{\text{eff}} = \sum_I \langle \alpha | \hat{V} | I \rangle \frac{1}{E_{\beta}^{(0)} - E_I^{(0)}} \langle I | \hat{V} | \beta \rangle, \quad (4)$$

where the zeroth-order energies in the denominator are

$$E_{\beta}^{(0)} = \langle \beta | \hat{H}^{(0)} | \beta \rangle, \quad (5)$$

$$E_I^{(0)} = \langle I | \hat{H}^{(0)} | I \rangle. \quad (6)$$

The effective Hamiltonian is then diagonalized to result in the MCQDPT2 state.

In the original MCQDPT2, the off-diagonal elements of the zeroth-order Hamiltonian in the state basis are nonzero. This leads to spurious behavior of the potential energy surfaces near the degeneracy of the reference function. Using the intermediate reference states that diagonalize the zeroth-order Hamiltonian,

$$\langle \alpha | \hat{H}^{(0)} | \beta \rangle = \delta_{\alpha\beta} E_{\beta}^{(0)}, \quad (7)$$

can address this problem. This modified version of MCQDPT2 is the extended MCQDPT2 (XMCQDPT2),<sup>31</sup> which was also applied to MS-CASPT2, resulting in the XMS-CASPT2 method.<sup>15</sup> An intermediate theory between MS-CASPT2 and XMS-CASPT2, i.e., extended dynamically weighted CASPT2, was also suggested, and it has been demonstrated that the theory performs well for geometries with large and small separations between electronic states.<sup>34</sup>

Multiconfiguration perturbation theories usually suffer from the intruder state problem.<sup>35-</sup>

<sup>37</sup> The intruder state is present when the denominator  $\Delta_I$  in the (X)MCQDPT2 expansion is close to zero such that

$$H_{\alpha\beta} = \sum_I \frac{N_I}{\Delta_I} \quad (8)$$

diverges. This problem can be circumvented by the intruder state avoidance (ISA) technique.<sup>35</sup>

With the ISA technique, the denominator is regularized as

$$\Delta_I \rightarrow \Delta_I + \frac{\tau}{\Delta_I}, \quad (9)$$

where  $\tau$  is the ISA parameter with a dimension  $E_h^2$ . We note that this corresponds to the imaginary shift technique in CASPT2.<sup>20,37</sup>

**Resolvent Fitting.** We now review the resolvent-fitting (table-driven) approximation in the (X)MCQDPT2 calculations.<sup>32</sup> This method considers the perturbation summations over the Slater determinants (resolvents) as a smooth function of the zeroth-order energy difference. This is always true when the ISA technique is employed. Then, the terms required for perturbation summations are interpolated rather than explicitly computed. We take the second term in the (X)MCQDPT2 expansion as an example:

$$H_{\alpha\beta}^{\text{eff}} = \sum_B c_{B\alpha} c_{B\beta} \sum_{ia'jb'} \frac{\Delta_{a'ib'j,B\beta} (ia' | jb') [2(a'i | b'j) - (a'j | b'i)]}{\Delta_{a'ib'j,B\beta}^2 + \tau}, \quad (10)$$

where the denominator is

$$\Delta_{a'ib'j,B\beta} = \varepsilon_{a'} - \varepsilon_i + \varepsilon_{b'} - \varepsilon_j + \Delta E_{B\beta}. \quad (11)$$

In the original (X)MCQDPT2, the latter summation is explicitly calculated. For brevity, we rewrite the latter sum as

$$S^{(0)}(\Delta E_{B\beta}) = \sum_{ia'jb'} \frac{\Delta_{a'ib'j,B\beta} (ia' | jb') [2(a'i | b'j) - (a'j | b'i)]}{\Delta_{a'ib'j,B\beta}^2 + \tau}. \quad (12)$$

Then, one can rewrite the contribution of this term to the effective Hamiltonian as

$$H_{\alpha\beta}^{\text{eff}} = \sum_B c_{B\alpha} c_{B\beta} S^{(0)}(\Delta E_{B\beta}). \quad (13)$$

Granovsky realized that this  $S^{(0)}(\Delta E_{B\beta})$  can be regarded as a smooth function of  $\Delta E_{B\beta}$  when the ISA technique is applied. Thus, it is possible to interpolate this function.<sup>32</sup> For interpolation, a helper grid  $\lambda$  is introduced. At each grid point  $\lambda_g$ ,  $S^{(0)}(\lambda_g)$  is evaluated as

$$S^{(0)}(\lambda_g) = \sum_{ia'jb'} \frac{\Delta_{a'ib'j,g}(ia' | jb')[2(a'i | b'j) - (a'j | b'i)]}{\Delta_{a'ib'j,g}^2 + \tau}, \quad (14)$$

where  $\Delta_{a'ib'j,g} = \varepsilon_{a'} - \varepsilon_i + \varepsilon_{b'} - \varepsilon_j + \lambda_g$ . The value of  $S^{(0)}$  is saved for each  $\lambda_g$ . The separation of  $\Delta\lambda = 0.05E_h$  is sufficient to achieve accuracy on the order of  $1.0 \times 10^{-7} E_h$ . In our implementation, we fixed the values of  $\lambda$  at all geometrical points. When evaluating the effective Hamiltonian, we loop over  $\alpha$ ,  $\beta$ , and  $B$ . The interpolant  $S^{(0)}(\Delta E_{B\beta})$  can be approximated by the Lagrangian interpolation as

$$S^{(0)}(\Delta E_{B\beta}) \approx \sum_g S^{(0)}(\lambda_g) W_g(\Delta E_{B\beta}), \quad (15)$$

where the interpolation weights  $W_g$  can be determined by arbitrary means. In our implementation, we use the eight-point polynomial interpolation, which means that  $N_{\text{fgrid}} = 8$  for each  $\Delta E_{B\beta}$ . The weights are

$$W_g(\Delta E_{B\beta}) = \prod_{h \neq g} \frac{\Delta E_{B\beta} - \lambda_h}{\lambda_g - \lambda_h}. \quad (16)$$

For computational efficiency, the interpolation coefficients are evaluated and stored before the (X)MCQDPT2 calculation.

An evaluation of Eq. 10 requires  $N_{\text{vir}}^2 N_{\text{core}}^2 N_{\text{det}} N_{\text{state}}^2$  and  $N_{\text{grid}} N_{\text{vir}}^2 N_{\text{core}}^2 + (N_{\text{fgrid}} + N_{\text{state}}) N_{\text{state}} N_{\text{det}}$  operations without and with the resolvent-fitting approximation, respectively. Therefore, the resolvent-fitted (X)MCQDPT2 is always favorable over the canonical (X)MCQDPT2, particularly when the numbers of determinants and states are large (see also numerical examples). Similarly, the most expensive three-particle term requires  $N_{\text{grid}} (N_{\text{core}} + N_{\text{vir}}) N_{\text{act}}^6 + (N_{\text{fgrid}} + N_{\text{state}}) N_{\text{act}}^6 N_{\text{det}} N_{\text{state}}$  operations (the XMS-CASPT2 and QD-

NEVPT2 analytical gradient algorithms require  $\frac{1}{8}N_{\text{state}}^2 N_{\text{det}} N_{\text{act}}^8$  operations in 4RDM evaluations).

Therefore, in principle, the cost for the (X)MCQDPT2 gradient can be comparable to that of the XMS-CASPT2 or QD-NEVPT2 gradients.

The full effective Hamiltonian element can be recast as

$$\begin{aligned}
H_{\alpha\beta}^{\text{eff}} &= \sum_B c_{B\alpha} c_{B\beta} \sum_g W_g(\Delta E_{B\beta}) S^{(0)}(\lambda_g) \\
&= \sum_g \left[ \sum_B c_{B\alpha} c_{B\beta} W_g(\Delta E_{B\beta}) \right] S^{(0)}(\lambda_g) \\
&\equiv \sum_g P_g^{\alpha\beta} S^{(0)}(\lambda_g),
\end{aligned} \tag{17}$$

where we have defined  $P_g^{\alpha\beta}$ , which is useful in formulating the analytical gradient theory.

Although we have presented an explicit form of the equation only for zero-particle terms, the one- to three-particle terms can be accelerated in the same way, as one can rewrite these terms as

$$H_{\alpha\beta}^{\text{eff},1} = \sum_B \sum_{ab} \langle \alpha | \hat{E}_{ab} | B \rangle c_{B\beta} S_{ab}^{(1)}(\Delta E_{B\beta}), \tag{18}$$

$$H_{\alpha\beta}^{\text{eff},2} = \sum_B \sum_{aba'b'} \langle \alpha | \hat{E}_{ab,a'b'} | B \rangle c_{B\beta} S_{ab,a'b'}^{(2)}(\Delta E_{B\beta}), \tag{19}$$

$$H_{\alpha\beta}^{\text{eff},3} = \sum_B \sum_{aba'b'a'b''} \langle \alpha | \hat{E}_{ab,a'b',a''b''} | B \rangle c_{B\beta} S_{ab,a'b',a''b''}^{(3)}(\Delta E_{B\beta}). \tag{20}$$

If the one-particle RDM term is evaluated with interpolation, we can rewrite the equation as

$$\begin{aligned}
H_{\alpha\beta}^{\text{eff},1} &= \sum_B \sum_{ab} \langle \alpha | \hat{E}_{ab} | B \rangle c_{B\beta} \sum_g W_g(\Delta E_{B\beta}) S_{ab}^{(1)}(\lambda_g) \\
&= \sum_{ab} \sum_g \left[ \sum_B \langle \alpha | \hat{E}_{ab} | B \rangle c_{B\beta} W_g(\Delta E_{B\beta}) \right] S_{ab}^{(1)}(\lambda_g). \\
&= \sum_{ab} \sum_g P_{ab,g}^{\alpha\beta} S^{(1)}(\lambda_g)
\end{aligned} \tag{21}$$

Then, the energy of the (X)MCQDPT2 state  $P$  is

$$E_P = \sum_{ab} \sum_g \sum_{\alpha\beta} T_{\alpha\beta}^P P_{ab,g}^{\alpha\beta} S^{(1)}(\lambda_g), \tag{22}$$

where  $T_{\alpha\beta}^P$  is defined as  $T_{\alpha\beta}^P = R_{\alpha p} R_{\beta p}$  and  $\mathbf{R}$  is the eigenvector of the effective Hamiltonian. We further define

$$\begin{aligned} P'_{ab,g} &= \sum_{\alpha\beta} T_{\alpha\beta}^P P_{ab,g}^{\alpha\beta} \\ &= \sum_{\alpha\beta} T_{\alpha\beta}^P \sum_B \langle \alpha | \hat{E}_{ab} | B \rangle c_{B\beta} W_g (\Delta E_{B\beta}). \end{aligned} \quad (23)$$

The evaluation of  $\mathbf{P}'$  requires  $N_{\text{act}}^2 N_{\text{det}} N_{\text{grid}} N_{\text{state}}^2$  operations. This quantity is directly related to the (X)MCQDPT2 energy and is valuable for analytical gradient theory.

**Analytical Gradient Theory.** Let us now derive the expressions for the pseudodensities and CI derivatives for the resolvent-fitted (X)MCQDPT2, which are necessary for evaluating the analytical gradient. The zero-particle energy is

$$\begin{aligned} E_P &= \sum_{\alpha\beta} T_{\alpha\beta}^P \sum_B c_{B\alpha} c_{B\beta} \sum_g S^{(0)}(\lambda_g) W_g \\ &= \sum_g P'_g S^{(0)}(\lambda_g). \end{aligned} \quad (24)$$

Here, we have defined

$$P'_g = \sum_{\alpha\beta} T_{\alpha\beta}^P \sum_B c_{B\alpha} c_{B\beta} W_g, \quad (25)$$

the computation of which requires  $N_{\text{det}} N_{\text{grid}} N_{\text{state}}^2$  operations. The expressions for the CI derivative are just

$$y_{B\alpha} = \sum_{\beta} T_{\alpha\beta}^P c_{B\beta} \sum_g S^{(0)}(\lambda_g) W_g, \quad (26)$$

$$y_{B\beta} = \sum_{\alpha} T_{\alpha\beta}^P c_{B\alpha} \sum_g S^{(0)}(\lambda_g) W_g. \quad (27)$$

The density matrices are also simply obtained. If one uses fixed grid points, the derivative with respect to  $\lambda$  is zero. Consequently, the weighting factor is solely a function of  $\Delta E_{B\beta}$ . This means

that the density matrix elements, except those from  $\Delta E_{B\beta}$ , have contributions only from  $S^{(0)}$ . For denominators, we write the Lagrangian as

$$\mathcal{L}_{\text{XMCQDPT2}} = E_P + Q_{a'ib'jg}^\tau (\varepsilon_{a'} - \varepsilon_i + \varepsilon_{b'} - \varepsilon_j + \lambda_g - \Delta_{a'ib'j,g}). \quad (28)$$

Then, the multiplier  $Q_{a'ib'jg}^\tau$  is

$$Q_{a'ib'jg}^\tau = \frac{\Delta_{a'ib'j,g}^2 - \tau}{\Delta_{a'ib'j,g}^2 + \tau} P'_g. \quad (29)$$

If  $\lambda$  is fixed at all molecular geometries (which is the case in our implementation), the density matrix elements are

$$\begin{aligned} d_{a'a'}^{\text{Fock}} &= d_{b'b'}^{\text{Fock}} = \sum_g Q_{a'ib'jg}^\tau, \\ d_{ii}^{\text{Fock}} &= d_{jj}^{\text{Fock}} = -\sum_g Q_{a'ib'jg}^\tau. \end{aligned} \quad (30)$$

The density matrix elements from the numerator are

$$\begin{aligned} D_{ia'jb'}^{(1)} &= \sum_g P'_g \frac{2(a'i | b'j) - (a'j | b'i)}{\varepsilon_{a'} - \varepsilon_i + \varepsilon_{b'} - \varepsilon_j + \lambda_g}, \\ D_{a'ib'j}^{(1)} &= \sum_g P'_g \frac{2(ia' | jb')}{\varepsilon_{a'} - \varepsilon_i + \varepsilon_{b'} - \varepsilon_j + \lambda_g}, \\ D_{a'jb'i}^{(1)} &= -\sum_g P'_g \frac{(ia' | jb')}{\varepsilon_{a'} - \varepsilon_i + \varepsilon_{b'} - \varepsilon_j + \lambda_g}. \end{aligned} \quad (31)$$

As we interpolate the  $S$ -values, the derivatives of the weights should contribute as

$$G_{B\beta} = \sum_{\alpha\beta} T_{\alpha\beta}^P \sum_B c_{B\alpha} c_{B\beta} \sum_g S^{(0)}(\lambda_g) \frac{\partial W_g}{\partial \Delta E_{B\beta}}, \quad (32)$$

and they can be formed simultaneously with the CI derivatives. This quantity then modifies the density matrices as

$$d_{aa}^{\text{Fock}} = G_{B\beta} \eta_a^B, \quad (33)$$

$$d_{ab}^{\text{Fock}} = -G_{B\beta} \langle \beta | \hat{E}_{ab} | \beta \rangle, \quad (34)$$

where  $\eta_a^B$  is the occupation number of orbital  $a$  in determinant  $B$ . The numerical differentiation of  $W_g$  with respect to  $\Delta E_{B\beta}$  works efficiently and accurately, although the analytical expression for  $\partial W_g / \partial \Delta E_{B\beta}$  could also be derived. With all these terms, one can evaluate the derivatives of the Lagrangian with respect to the orbital parameters as

$$\mathbf{Y} = 2 \left[ \mathbf{h}\mathbf{d}^{(0)} + \mathbf{u}\mathbf{d}^u + \mathbf{f}\mathbf{d}^{\text{Fock}} + \mathbf{g}(\mathbf{d}^u)\mathbf{d}^{\text{clo}} + \mathbf{g}(\mathbf{d}^{\text{Fock}})\mathbf{d}^{(0)} + \sum_{kl} \mathbf{D}^{kl} \mathbf{K}^{lk} \right], \quad (35)$$

where  $\mathbf{d}^{(0)}$  and  $\mathbf{D}^{(0)}$  are the one- and two-electron density matrices of the reference function,  $D_{rs}^{kl} = \frac{1}{2} [D_{rkls}^{(0)} + D_{rkls}^{(1)}]$ , and  $K_{rs}^{lk} = (rl | sk)$ . The derivatives  $\mathbf{Y}$  and  $\mathbf{y}$  are then used in solving the so-called  $Z$ -vector equation in the same manner as for the canonical XMCQDPT2 analytical gradient.<sup>30</sup>

**Density Fitting in Y Evaluation.** An evaluation of the two-particle density matrix,  $\mathbf{D}$ , is necessary for gradient evaluation. Unfortunately, this matrix is  $(N_{\text{act}} + N_{\text{core}})^2 (N_{\text{vir}} + N_{\text{act}})^2$  in size, being 80 GB when  $N_{\text{act}} + N_{\text{core}} = 100$  and  $N_{\text{vir}} + N_{\text{act}} = 1000$ . This makes the algorithm (unnecessarily) costly in terms of memory use. We have avoided the storage of the full  $\mathbf{D}$  by exploiting the density-fitting algorithm in evaluating the last term in Eq. 35, i.e.,  $\sum_{kl} \mathbf{D}^{kl} \mathbf{K}^{lk}$ .

One can evaluate the  $\sum_{kl} \mathbf{D}^{kl} \mathbf{K}^{lk}$  term as in Eqs. 24 to 30 in Ref. 16. The  $\mathbf{D}$  tensor is contracted with the density-fitting integral (Eq. 28 in Ref. 16) to form the intermediate tensor  $\mathbf{V}$  as

$$V_{si}^p = \sum_{jt} D_{isjt} \sum_Q J_{PQ}^{-1}(Q | jt) \equiv \sum_{jt} D_{isjt} d_{jt}^p, \quad (36)$$

where  $\mathbf{J}$  is the electron repulsion integral over an auxiliary basis, a central quantity for using the Coulomb metric in density fitting.<sup>38</sup> The zero-particle terms (Eq. 31) contribute to the largest

subtensor to  $\mathbf{D}$ . The full zero-particle part of  $\mathbf{D}$  has  $N_{\text{core}}^2 (N_{\text{vir}} + N_{\text{act}})^2$  elements. Instead of storing the entire matrix, we loop over  $i$  and  $j$  and allocate the submatrix with fixed  $\{i, j\}$ , the size of which is only  $(N_{\text{act}} + N_{\text{vir}})^2$ . Then, one forms tensor  $\mathbf{V}$  by performing the contraction in Eq. 36 separately for each pair  $\{i, j\}$ . The size of the largest  $\mathbf{D}$  matrix stored in the memory is  $(N_{\text{act}} + N_{\text{core}})^2 (N_{\text{vir}} + N_{\text{act}}) N_{\text{act}}$  for two- and three-particle terms. Overall, storing only submatrices of  $\mathbf{D}$  results in the saving of memory by a factor of  $\frac{N_{\text{act}}}{N_{\text{act}} + N_{\text{vir}}}$ . When a large basis set is used,  $N_{\text{vir}} \gg N_{\text{act}}$ , which results in large savings in terms of memory.

### 3. NUMERICAL EXAMPLES

This section presents numerical examples of the resolvent-fitted XMCQDPT2 analytical gradient theory for optimizing the conical intersection geometries in RPSB6 with the (12e, 12o) active space. We then demonstrate how the current algorithm performs for systems with many electronic states and the parallel efficiency in and across computer nodes. The density-fitting approximation is used in all calculations. In all XMCQDPT2 calculations, we used an ISA parameter of  $0.02 E_h^2$ .<sup>35</sup>

**Minimum Energy Conical Intersection Optimizations of RPSB6.** An investigation of photoisomerization of the retinal protonated Schiff base (RPSB) is essential in vision studies.<sup>39-42</sup> Many truncated models of the RPSB have been employed to inspect the photoisomerization of rhodopsin.<sup>39-42</sup> Two photodeactivation pathways are considered responsible: the twisting of the 11–12 and 13–14 double bonds. In the author and Shiozaki’s previous benchmarks using XMS-CASPT2 with the cc-pVDZ basis set,<sup>43</sup> the 13–14 minimum energy conical intersection (MECI)

in RPSB6 was thermally unreachable at the Franck–Condon point. Here, we present the resolvent-fitted XMCQDPT2 optimization of the MECIs in RPSB6 using the cc-pVTZ basis set<sup>44</sup> and its corresponding JKFIT basis set,<sup>45</sup> which resulted in 1108 basis functions. We include the three lowest singlet states in the SA-CASSCF and XMCQDPT2 calculations. We perform MECI searches with the gradient projection method.<sup>46</sup> We note that we could not afford the computational cost with cc-pVTZ in our previous XMS-CASPT2 benchmark, and the XMS-CASPT2/cc-pVDZ results are compared.

The structures of the resulting all-*trans*  $S_0$  equilibrium geometry, i.e., the 11–12 and 13–14 MECIs, are shown in Figure 1. First, the vertical excitation energy is 2.14 eV, which is approximately 0.32 eV lower than the XMS-CASPT2/cc-pVDZ value (2.46 eV). To check the main reason behind this discrepancy, we optimize the  $S_0$  geometry with XMCQDPT2/cc-pVDZ. The resulting vertical excitation energy is 2.27 eV, which is 0.13 eV higher than the cc-pVTZ value. This result means that the XMCQDPT2 vertical excitation energy of RPSB6 is very sensitive to the basis set selection. The geometry optimization with XMS-CASPT2(D)/cc-pVTZ yields vertical excitation energies of 2.18 eV and 2.41 eV with an imaginary shift of  $0.2 E_h$  and a real shift of  $0.5 E_h$ , respectively. This implies that the vertical excitation energy is highly shift-dependent as well. The previous results on various shifts in CASPT2 calculations show that a high real shift leads to severe changes in the computational results. Therefore, lower values of the imaginary shift (equivalent to the ISA parameter in XMCQDPT2) are recommended.<sup>20,37</sup> Our selection of the ISA parameter corresponds to the imaginary shift of  $0.14 E_h$ , and we can assume that the XMCQDPT2 results are closer to the zero-shift limit.

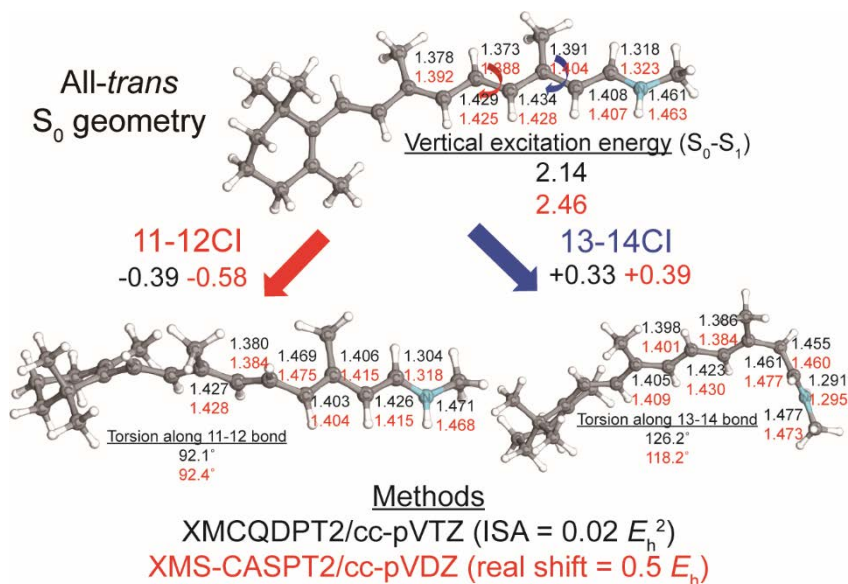
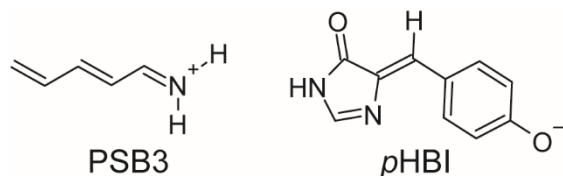


**Figure 1.** Optimized all-*trans*  $S_0$  and MECI structures of RPSB6. All bond lengths are shown in Å. For comparative purposes, the XMS-CASPT2/cc-pVDZ geometrical parameters from Ref. <sup>43</sup> are shown in red. The energies with respect to the  $S_1$  energy at the Franck–Condon point (in eV) are also shown. The molecular graphics were generated using the IboView software.<sup>47,48</sup>

The energies of the 11–12 MECI and 13–14 MECI are 0.39 eV lower and 0.33 eV higher than the  $S_1$  energy at the Franck–Condon point, respectively. These differences are smaller than the XMS-CASPT2/cc-pVDZ values (0.58 eV and 0.39 eV), but the “directions” of the energetic differences are the same. This finding supports the idea that the trends in the MECI energies with XMCQDPT2 will be similar to the XMS-CASPT2 trends and validates the previous prediction that the 11–12 MECI will be more stable than the 13–14 MECI in RPSB6. The geometrical parameters for XMS-CASPT2/cc-pVDZ and XMCQDPT2/cc-pVTZ are also similar, except for some parameters, such as the torsion along the 13–14 bond at the 13–14 MECI, with a difference of ~8 deg. Overall, XMCQDPT2 with a resolvent-fitting approximation yields MECI optimization results similar to the XMS-CASPT2 results for RPSB6.

**Computational Cost.** Next, let us discuss the computational cost for the resolvent-fitted XMCQDPT2 calculations. We display the wall time associated with the significant computational steps in Table 1 for two test systems: the truncated rhodopsin protonated Schiff base model penta-2,4-dieniminium cation (PSB3) with the cc-pV5Z basis set and the green fluorescent protein chromophore model *para*-hydroxybenzilideneimidazolin-5-one (*p*HBI) with the aug-cc-pVTZ basis set (see Scheme 1 for their structures). Although the resolvent-fitting approximation is applied, the wall time for the (12*e*, 11*o*) *p*HBI anion (805 basis functions) is approximately 20 times longer than that for (6*e*, 6*o*) PSB3 (986 basis functions). This is in stark contrast to the internally contracted theories. The parts that are the most sensitive to the active space size in XMS-CASPT2 or QD-NEVPT2 are computations of RDMs and CI derivative evaluations. In resolvent-fitted XMCQDPT2, the energy evaluations, pseudodensities, and CI derivatives are strongly dependent on the number of determinants, as it is an uncontracted theory. For example, the calculation of *p*HBI required ~30 times more wall time than did PSB3. However, because the size of the CASCI space in *p*HBI is ~500 times larger than that of PSB3, one can see that the resolvent-fitting approximation is quite efficient in separating the computational efforts that are dependent and not dependent on the active space.



**Scheme 1.** Structures of PSB3 and pHBI anion.

**Table 1.** Wall time for the XMCQDPT2 energy and gradient evaluations.<sup>a</sup>

|                                    | PSB3     | pHBI anion  |
|------------------------------------|----------|-------------|
| Basis set                          | cc-pV5Z  | aug-cc-pVTZ |
| Active space                       | (6e, 6o) | (12e, 11o)  |
| Number of states                   | 3        | 3           |
| Number of basis functions          | 986      | 805         |
| Denominator, table, and gradient   | 6        | 9           |
| 3-index integrals                  | 5        | 7           |
| Active integrals                   | 16       | 41          |
| MCQDPT2 energy                     | 55       | 1832        |
| Pseudodensities and CI derivatives | 533      | 13128       |
| Orbital gradient evaluation        | 13       | 16          |
| Z-vector equation                  | 214      | 833         |
| Derivative integral contraction    | 21       | 18          |
| Total time                         | 863      | 15885       |

<sup>a</sup> These times are measured using 18 physical cores in an Intel Xeon Gold 6140 processor (2.3 GHz).

**Inclusion of Many States.** The resolvent-fitting approximation decouples the computational cost proportional to the number of orbitals and determinants from the number of states. Therefore, the inclusion of many states is possible without a significant increase in the computational cost. In contrast, the computational cost is almost proportional to  $N_{\text{state}}$  or  $N_{\text{state}}^2$  in MS-CASPT2 or QD-NEVPT2 and  $N_{\text{state}}$  in the canonical XMCQDPT2. Here, we test the performance of our XMCQDPT2 (which computes perturbation in the uniform FOIS) analytical gradient algorithm when treating a large number of electronic states with  $(6e, 5o)$ ,  $(8e, 7o)$ ,  $(10e, 9o)$ , and  $(12e, 11o)$  active spaces in the *p*HBI anion. We test the cases of  $N_{\text{state}} = 3$  to 10. The relative timings compared to  $N_{\text{state}} = 3$  are shown in Figure 2.

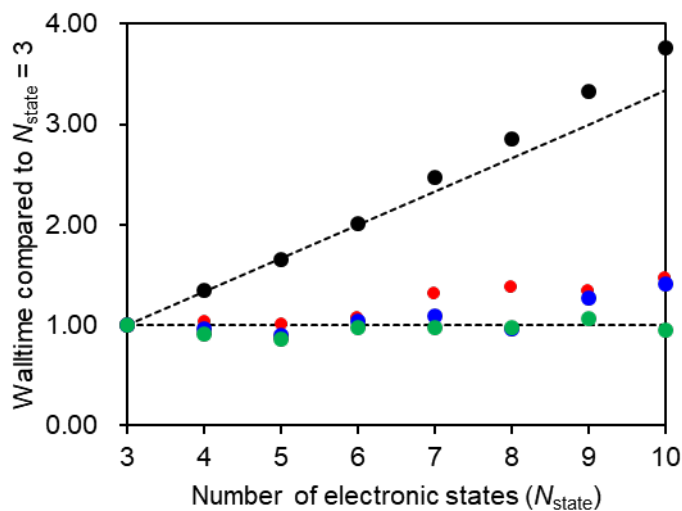


**Figure 2.** Relative wall time of the XMCQDPT2 analytical gradient using various electronic states ( $N_{\text{state}}$ ) compared to  $N_{\text{state}} = 3$ . The relative wall times for the  $(12e, 11o)$ ,  $(10e, 9o)$ ,  $(8e, 7o)$ , and  $(6e, 5o)$  active spaces are shown in black, red, blue, and green, respectively. For comparative purposes, the ideal wall times proportional to and constant with respect to  $N_{\text{state}}$  are also displayed (dashed lines).

From the  $(6e, 5o)$  to  $(10e, 9o)$  active spaces, the wall times do not significantly increase with respect to the number of states. The most dominant computational effort in the resolvent-fitted XMCQDPT2 is for the three-particle term, which requires

$$N_{\text{grid}}(N_{\text{core}} + N_{\text{vir}})N_{\text{act}}^6 + (N_{\text{fgid}} + N_{\text{state}})N_{\text{act}}^6 N_{\text{det}} N_{\text{state}} \quad (37)$$

operations. When  $N_{\text{act}}$  and  $N_{\text{det}}$  are small, the former term dominates, which is the reason for the small increase in the computational cost with increasing  $N_{\text{state}}$ . However, there are contributions from the latter term, and when the  $(10e, 9o)$  and  $(8e, 7o)$  active spaces are used, the computational cost slightly increases.

With the  $(12e, 11o)$  active space, the computational cost is almost proportional to  $N_{\text{state}}$  [ $a = 1.08$  with the least-squares fit to the curve  $(N_{\text{state}}/3)^a$ ]. In this case, the wall times for both evaluations of the energy and pseudodensity are almost proportional to  $N_{\text{state}}$  or slightly higher, as the latter term in Eq. (37) dominates the overall computational cost. If  $N_{\text{fgid}}$  (which is 8 in our implementation) is smaller than or close to  $N_{\text{state}}$ , the computational cost will be higher than linear.

Overall, the computational cost for the XMCQDPT2 analytical gradient remains almost unchanged with increasing  $N_{\text{state}}$  when the active space is small, as the portion proportional to the number of states is minor. However, when the active space has more than  $\sim 10$  orbitals (or  $\sim 100$  000 determinants), the cost is proportional to the number of states. Of course, when one employs the XMCQDPT2 analytical gradient for applications such as geometry optimizations or direct dynamics simulations, the stability and continuity of the active space are sensitive to the number of states. Therefore, one should carefully check the numerical stability when one includes a large number of states.

**Parallel Efficiency.** Finally, we comment on the parallel efficiency of the current algorithm with

the OpenMP/MPI hybrid approach. OpenMP and MPI are responsible for intranode and internode parallelization, respectively. The zero-particle term is distributed to the MPI process by closed (core) indices, and the evaluations for each active or virtual index are distributed in each core with OpenMP. For one- to three-particle terms, the MPI processes are distributed by two active indices ( $N_{\text{act}}^2$ ), except for the virtual-virtual term in the one-particle term

$$H_{\alpha\beta}^{\text{eff}} = -\frac{1}{2} \sum_{pq} \langle A | \hat{E}_{pq} | B \rangle \sum_{ia'b'} \frac{(ia' | pb') [2(a'i | b'q) - (a'q | b'i)]}{\varepsilon_{a'} - \varepsilon_i + \varepsilon_{b'} - \varepsilon_q + \Delta E_{B\beta}} \quad (38)$$

distributed by  $a'$  to reduce the memory requirement for temporary storage of the pseudodensities. In each process, the one-particle term is distributed by closed (core) or virtual indices in each core, and one-particle virtual-virtual and two- and three-particle terms are distributed by two active indices ( $N_{\text{act}}^2$ ) in each core. These distributions can deteriorate the parallel efficiency when one uses many MPI processes, but this was not the case for the current tests. We tested the parallel efficiency for (6e, 6o) PSB3 with cc-pV5Z and (12e, 11o) pHBI with aug-cc-pVTZ. The tests were performed using an Intel Xeon Gold 6140 processor (2.3 GHz) connected to an Intel OmniPath 100 Series network node.

The current status of multithreading and MPI parallelization is shown in Figure 3, along with Amdahl's law fitting. In the case of multithreading (Figure 3a), Amdahl's law coefficient  $A$  was 0.88 and 0.95, respectively, for PSB3 and pHBI. There was an anomalous speedup behavior, particularly for PSB3, because we distribute the process with respect to two active orbitals. In PSB3 and pHBI,  $N_{\text{act}}^2$  is 36 and 121, respectively, and the load unbalances are significant when the number of threads is larger than 12. We distribute the jobs statistically, which suggests that the dynamic distributions might improve this behavior. The MPI parallelization (Figure 3b) yielded an  $A$  value of 0.93 for PSB3 and pHBI. Unlike XMS-CASPT2 or QD-NEVPT2, the parallel efficiency of the algorithm did not significantly degrade when using a large active space. For

massively parallel applications, the distributions of the procedure should be redesigned, which will be left for future investigations.

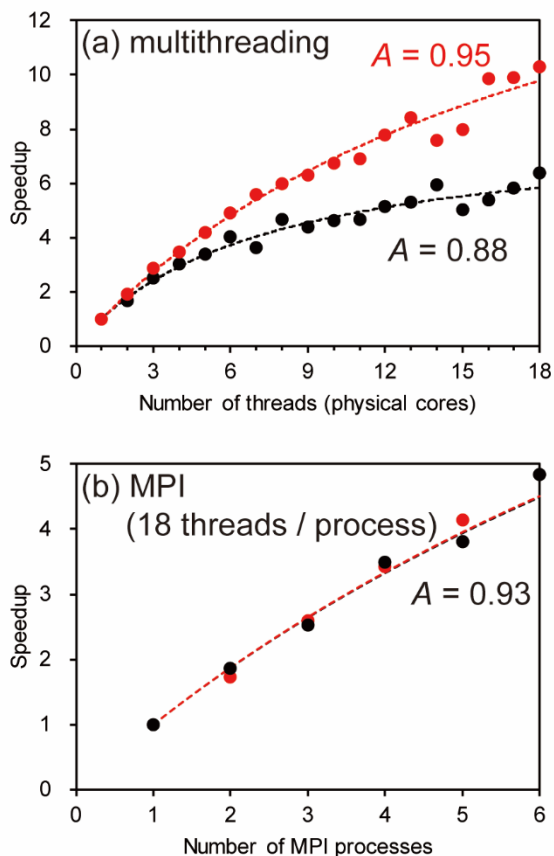


**Figure 3.** Parallel performance of the resolvent-fitted XMCQDPT2 gradient of PSB3 [(6e, 6o), cc-pV5Z (986 basis functions), black] and pHBI [(12e, 11o), aug-cc-pVTZ (805 basis functions), red]: (a) multithreading performance and (b) internode MPI performance. The data are fitted into Amdahl's law [speedup =  $1/(1 - A + A/N)$ , where  $N$  is the number of threads or processes], and the coefficient  $A$  is given.

## 4. SUMMARY

In this work, we presented implementations of the analytical gradient of resolvent-fitted XMCQDPT2. We demonstrated its applicability for optimizing the geometries of large systems with moderate-sized active spaces. The resolvent-fitting approximation enables geometry optimizations with moderate-sized CASCI spaces up to  $(12e, 12o)$ . Furthermore, we parallelized the algorithm using the OpenMP/MPI hybrid strategy. The source codes for the analytical gradient of canonical and resolvent-fitted (X)MCQDPT2 are distributed as a patch on open-source BAGEL (<http://github.com/qsimulate-open/bagel>) version Feb 10 2021 at <http://sites.google.com/view/cbnuqbc/codes> under a GPU-v3 license.

## ACKNOWLEDGMENTS

This work was supported by a National Research Foundation (NRF) grant funded by the Korean government (MSIT) (Grant 2019R1C1C1003657) and by the POSCO Science Fellowship of POSCO TJ Park Foundation.

## REFERENCES

1. Andersson, K.; Malmqvist, P.-Å.; Roos, B. O.; Sadlej, A. J.; Wolinski, K., Second-Order Perturbation Theory with a CASSCF Reference Function. *J. Phys. Chem.* **1990**, *94*, 5483-5488.
2. Andersson, K.; Malmqvist, P.-Å.; Roos, B. O., Second-Order Perturbation Theory with a Complete Active Space Self-Consistent Field Reference Function. *J. Chem. Phys.* **1992**, *96*, 1218-1226.
3. Angeli, C.; Cimiraglia, R.; Malrieu, J.-P., n-electron Valence State Perturbation Theory:

A Spinless Formulation and an Efficient Implementation of the Strongly Contracted and of the Partially Contracted Variants. *J. Chem. Phys.* **2002**, *117*, 9138-9153.

4. Angeli, C.; Cimiraglia, R.; Malrieu, J.-P., N-electron valence state perturbation theory: a fast implementation of the strongly contracted variant. *Chem. Phys. Lett.* **2001**, *350*, 297-305.

5. Angeli, C.; Cimiraglia, R.; Evangelisti, S.; Leininger, T.; Malrieu, J.-P., Introduction of n-electron Valence States for Multireference Perturbation Theory. *J. Chem. Phys.* **2001**, *114*, 10252-10264.

6. Hirao, K., Multireference Møller-Plesset Method. *Chem. Phys. Lett.* **1992**, *190*, 374-380.

7. Hirao, K., State-Specific Multireference Møller-Plesset Perturbation Treatment for Singlet and Triplet Excited States, Ionized States and Electron Attached States of H<sub>2</sub>O. *Chem. Phys. Lett.* **1993**, *201*, 59-66.

8. Hirao, K., Multireference Møller-Plesset Perturbation Theory for High-Spin Open-Shell Systems. *Chem. Phys. Lett.* **1992**, *196*, 397-403.

9. Nakano, H., Quasidegenerate perturbation theory with multiconfigurational self-consistent-field reference functions. *J. Chem. Phys.* **1993**, *99*, 7983-7992.

10. Coe, J. D.; Levine, B. G.; Martínez, T. J., Ab Initio Molecular Dynamics of Excited-State Intramolecular Proton Transfer Using Multireference Perturbation Theory. *J. Phys. Chem. A* **2007**, *111*, 11302-11310.

11. Levine, B. G.; Coe, J. D.; Martínez, T. J., Optimizing Conical Intersections without Derivative Coupling Vectors: Application to Multistate Multireference Second-Order Perturbation Theory (MS-CASPT2). *J. Phys. Chem. B* **2008**, *112*, 405-413.

12. Park, J. W.; Shiozaki, T., On-the-Fly CASPT2 Surface-Hopping Dynamics. *J. Chem. Theory Comput.* **2017**, *13*, 3676-3683.

13. Park, J. W.; Al-Saadon, R.; MacLeod, M. K.; Shiozaki, T.; Vlaisavljevich, B., Multireference Electron Correlation Methods: Journeys along Potential Energy Surfaces. *Chem. Rev.* **2020**, *120*, 5878-5909.
14. Celani, P.; Werner, H.-J., Analytical Energy Gradients for Internally Contracted Second-Order Multireference Perturbation Theory. *J. Chem. Phys.* **2003**, *119*, 5044-5057.
15. Shiozaki, T.; Gyórfy, W.; Celani, P.; Werner, H.-J., Communication: Extended Multi-State Complete Active Space Second-Order Perturbation Theory: Energy and Nuclear Gradients. *J. Chem. Phys.* **2011**, *135*, 081106.
16. Gyórfy, W.; Shiozaki, T.; Knizia, G.; Werner, H.-J., Analytical Energy Gradients for Second-Order Multireference Perturbation Theory using Density Fitting. *J. Chem. Phys.* **2013**, *138*, 104104.
17. MacLeod, M. K.; Shiozaki, T., Communication: Automatic Code Generation Enables Nuclear Gradient Computations for Fully Internally Contracted Multireference Theory. *J. Chem. Phys.* **2015**, *142*, 051103.
18. Vlaisavljevich, B.; Shiozaki, T., Nuclear Energy Gradients for Internally Contracted Complete Active Space Second-Order Perturbation Theory: Multistate Extensions. *J. Chem. Theory Comput.* **2016**, *12*, 3781-3787.
19. Park, J. W.; Shiozaki, T., Analytical Derivative Coupling for Multistate CASPT2 Theory. *J. Chem. Theory Comput.* **2017**, *13*, 2561-2570.
20. Park, J. W.; Al-Saadon, R.; Strand, N. E.; Shiozaki, T., Imaginary Shift in CASPT2 Nuclear Gradient and Derivative Coupling Theory. *J. Chem. Theory Comput.* **2019**, *15*, 4088-4098.
21. Park, J. W., Single-State Single-Reference and Multistate Multireference Zeroth-Order Hamiltonians in MS-CASPT2 and Conical Intersections. *J. Chem. Theory Comput.* **2019**, *15*,

3960-3973.

22. Song, C.; Neaton, J. B.; Martínez, T. J., Reduced Scaling Formulation of CASPT2 Analytical Gradients Using the Supporting Subspace Method. *J. Chem. Phys.* **2021**, *154*, 014103.
23. Park, J. W., Analytical Gradient Theory for Strongly Contracted (SC) and Partially Contracted (PC) N-Electron Valence State Perturbation Theory (NEVPT2). *J. Chem. Theory Comput.* **2019**, *15*, 5417-5425.
24. Park, J. W., Analytical Gradient Theory for Quasidegenerate N-Electron Valence State Perturbation Theory (QD-NEVPT2). *J. Chem. Theory Comput.* **2020**, *16*, 326-339.
25. Nishimoto, Y., Analytic First-Order Derivatives of Partially Contracted N-Electron Valence State Second-Order Perturbation Theory (PC-NEVPT2). *J. Chem. Phys.* **2019**, *151*, 114103.
26. Nishimoto, Y., Locating Conical Intersections Using the Quasidegenerate Partially and Strongly Contracted NEVPT2 Methods. *Chem. Phys. Lett.* **2020**, *744*, 137219.
27. Nishimoto, Y., Analytic Gradients for Restricted Active Space Second-Order Perturbation Theory (RASPT2). *J. Chem. Phys.* **2021**, *154*, 194103.
28. Nakano, H.; Hirao, K.; Gordon, M. S., Analytic energy gradients for multiconfigurational self-consistent field second-order quasidegenerate perturbation theory (MC-QDPT). *J. Chem. Phys.* **1998**, *108*, 5660-5669.
29. Nakano, H.; Otsuka, N.; Hirao, K., Analytical Energy Gradients for Second-Order Multireference Perturbation Theory. In *Recent Advances in Computational Chemistry*, Hirao, K., Ed. World Scientific: Singapore, 1999; Vol. 4, pp 131-160.
30. Park, J. W., Analytical First-Order Derivatives of Second-Order Extended Multiconfiguration Quasi-Degenerate Perturbation Theory (XMCQDPT2): Implementation and Application. *J. Chem. Theory Comput.* **2020**, *16*, 5562-5571.

31. Granovsky, A. A., Extended Multi-Configuration Quasi-Degenerate Perturbation Theory: The New Approach to Multi-State Multi-Reference Perturbation Theory. *J. Chem. Phys.* **2011**, *134*, 214113.
32. Granovsky, A. A. Table-Driven Implementation of the Multireference Perturbation Theories at Second Order. [http://classic.chem.msu.su/gran/gamess/table\\_qdpt2.pdf](http://classic.chem.msu.su/gran/gamess/table_qdpt2.pdf) (accessed Jun 8, 2021).
33. Nakano, H., MCSCF Reference Quasidegenerate Perturbation Theory with Epstein--Nesbet Partitioning. *Chem. Phys. Lett.* **1993**, *207*, 372-378.
34. Battaglia, S.; Lindh, R., Extended Dynamically Weighted CASPT2: the Best of Two Worlds. *J. Chem. Theory Comput.* **2020**, *16*, 1555-1567.
35. Witek, H. A.; Choe, Y. K.; Finley, J. P.; Hirao, K., Intruder State Avoidance Multireference Moller-Plesset Perturbation Theory. *J. Comput. Chem.* **2002**, *23*, 957-965.
36. Roos, B. O.; Andersson, K., Multiconfigurational Perturbation Theory With Level Shift - the Cr<sub>2</sub> Potential Revisited. *Chem. Phys. Lett.* **1995**, *245*, 215-223.
37. Forsberg, N.; Malmqvist, P. Å., Multiconfiguration Perturbation Theory with Imaginary Level Shift. *Chem. Phys. Lett.* **1997**, *274*, 196-204.
38. Dunlap, B. I.; Connolly, J. W. D.; Sabin, J. R., On Some Approximations in Applications of  $X\alpha$  Theory. *J. Chem. Phys.* **1979**, *71*, 3396-3402.
39. Fantacci, S.; Migani, A.; Olivucci, M., CASPT2//CASSCF and TDDFT//CASSCF Mapping of the Excited State Isomerization Path of a Minimal Model of the Retinal Chromophore. *J. Phys. Chem. B* **2004**, *108*, 1208-1213.
40. Gozem, S.; Schapiro, I.; Ferré, N.; Olivucci, M., The Molecular Mechanism of Thermal Noise in Rod Photoreceptors. *Science* **2012**, *337*, 1225-1228.

41. Gozem, S.; Luk, H. L.; Schapiro, I.; Olivucci, M., Theory and Simulation of the Ultrafast Double-Bond Isomerization of Biological Chromophores. *Chem. Rev.* **2017**, *117*, 13502-13565.
42. Manathunga, M.; Yang, X.; Orozco-Gonzalez, Y.; Olivucci, M., Impact of Electronic State Mixing on the Photoisomerization Time Scale of the Retinal Chromophore. *J. Phys. Chem. Lett.* **2017**, *8*, 5222-5227.
43. Park, J. W.; Shiozaki, T., On the Accuracy of Retinal Protonated Schiff Base Models. *Mol. Phys.* **2018**, *116*, 2583-2590.
44. Dunning, T. H., Gaussian basis sets for use in correlated molecular calculations. I. The atoms boron through neon and hydrogen. *J. Chem. Phys.* **1989**, *90*, 1007-1023.
45. Weigend, F., A Fully Direct RI-HF Algorithm: Implementation, Optimised Auxiliary Basis Sets, Demonstration of Accuracy and Efficiency. *Phys. Chem. Chem. Phys.* **2002**, *4*, 4285-4291.
46. Bearpark, M. J.; Robb, M. A.; Schlegel, H. B., A Direct Method for the Location of the Lowest Energy Point on a Potential Surface Crossing. *Chem. Phys. Lett.* **1994**, *223*, 269-274.
47. Knizia, G.; Klein, J. E. M. N., Electron Flow in Reaction Mechanisms—Revealed from First Principles. *Angew. Chem. Int. Ed.* **2015**, *54*, 5518-5522.
48. Knizia, G., Intrinsic Atomic Orbitals: An Unbiased Bridge between Quantum Theory and Chemical Concepts. *J. Chem. Theory Comput.* **2013**, *9*, 4834-4843.